Failure locus of fiber-reinforced composites under transverse compression and out-of-plane shear

Essam Totry , Carlos González , Javier LLorca

Departamento de Ciencia de Materiales, Universidad Politécnica de Madrid, E.T.S. de Ingenieros de Caminos, 28040 Madrid, Spain
Instituto Madrileño de Estudios Avanzados en Materiales (IMDEA-Materiales), E.T.S. de Ingenieros de Caminos, 28040 Madrid, Spain

Abstract

The failure locus a fiber-reinforced composite lamina, made up of 50 vol.% of carbon fibers embedded in an epoxy matrix, is computed under transverse compression and out-of-plane shear, a stress state whose experimental reproduction is highly complex. The mechanical response was obtained by the finite element method of a representative volume element of the lamina, which explicitly takes into account the fibers and the matrix in the lamina. The actual deformation and failure mechanisms experimentally observed in the matrix, fibers and interfaces were included in the simulations through the appropriate constitutive equations. Two sets of simulations were performed, assuming that the fiber/matrix interface was either strong or weak. The corresponding failure loci were compared with those given by three failure criteria for composites (Hashin, Puck and LaRC) which provide reasonable predictions in other multiaxial stress states. The estimations of the failure criteria were largely consistent with the numerical simulations in the composites with a strong interface but overestimated the composite strength when the interface was weak because the effect of interface decohesion (which becomes dominant) was not taken into account. These results point out the need to include interface fracture in the failure criteria for composites.

Keywords: A. Polymer-matrix composites; B. Mechanical properties; B. Modeling; C. Failure criterion

1. Introduction

Most materials exhibit a limited number of physical failure mechanisms upon deformation. For instance, engineering metallic alloys normally fail by a ductile process involving the nucleation, growth an coalescence of cavities [1]. Deformation of bulk metallic glasses at ambient temperature results in the localization of the strain into strips of nanometer-thickness and macroscopic length [2,3], while glassy and semi-crystalline polymers fail below the glass transition temperature by the formation of crazes and/or shear bands . These mechanisms can be taken into account in the analysis of the mechanical behavior through the respective failure criteria, obtained from phenomenological or micromechanical considerations, which establish the stress state at a given material point leading to the onset of damage. This task is relatively simple in homogeneous and isotropic materials, as only one or two failure mechanisms are active.

However, fiber-reinforced composites do not follow this trend and present completely different failure modes as a function of the loading direction and stress-state. For instance, a composite lamina made up of a polymeric matrix uniaxially reinforced with glass or carbon fibers presents four different physical fracture mechanisms depending on the loading mode [6]: tensile deformation in the longitudinal direction leads to fiber fracture while compression in the same direction induces failure by localized fiber

buckling. Tensile deformation perpendicular to the fibers results in matrix cracking, and transverse compression or shear deformation triggers fracture by the formation of matrix shear bands. Moreover, the different failure mechanisms are coupled and, for instance, the longitudinal compressive strength is severely reduced in presence of shear stresses in the longitudinal direction . Finally, failure criteria applicable to laminates should take into account the decohesion between individual plies.

Accurate and reliable failure criteria are necessary to take full advantage of the mechanical properties of advanced composites. A recent effort to assess the state-of-the-art in this matter, the World Wide Failure Exercise , compared the results provided by nineteen different failure criteria with benchmark experimental results on carbon- and glass-fiber laminates. The comparison showed that the predictions of many theories differed significantly from the experimental results (particularly under multiaxial stress states involving fracture by matrix and/or fiber compression), and ranked the available theories according to their ability to predict (a) biaxial lamina strength, (b) initial and final biaxial laminate strength, and (c) deformation of laminates. However, more precise conclusions regarding to the theory which best reproduces the physical failure mechanisms as well as the mechanical strength were limited by the scarcity of experimental results for multiaxial stress states, the experimental scatter (which sometimes impedes discrimination among the different theoretical predictions), and the phenomenological nature of most models. Evidently, more experimental results will help to clarify the situation but this approach is expensive and, in addition, mechanical testing composite lamina under multiaxial loading is complex due to different problems (buckling, free edge effects, failures at end constraints). As a result, the number of stress states that can be checked experimentally is not large enough to validate the failure criteria.

Another approach is resorting to virtual testing by means of computational micromechanics . This simulation strategy is very well suited to determine the mechanical behavior of composite lamina until fracture, and it based on the numerical simulation of a representative volume element (RVE) of the composite microstructure, which explicitly takes into account the fibers, matrix and interfaces in the lamina. The actual fracture mechanisms experimentally observed in the matrix, fibers and interfaces are included in the simulations through the appropriate constitutive equations. Recent examples includes the simulation of the fracture behavior perpendicular to the fibers of Ti/SiC composite panels at ambient and elevated temperature or the failure of fiber-reinforced polymer lamina under transverse compression [16]. In addition, complex multiaxial stress states (which cannot be obtained experimentally) are available using the appropriate boundary conditions. Thus this approach provides full control of the constituent properties, spatial distribution and loading, eliminating many sources of experimental error, and it can be used to assess the validity of the failure criteria or to develop new ones.

Computational micromechanics is used in this investigation to compute the failure locus of a composite lamina, made up of 50 vol.% of carbon fibers embedded in an epoxy matrix, which is subjected to transverse compression and out-of-plane shear, a biaxial stress state whose experimental reproduction is highly complex. The influence of the interface strength on the composite behavior is assessed and the predictions of the failure locus are compared with various failure criteria in composites with strong and weak interfaces.

2. Failure criteria under transverse compression

Hashin recognized more than 25 years ago that the coexistence of various physical mechanisms of failure in composites implied the use of different failure criteria as a function of the dominant stress state. He distinguished between fiber- and matrix-dominated fracture, and each one was further subdivided into tensile and compressive modes. Furthermore, he assumed that failure was due to the normal and tangential stresses acting on the fracture plane, which is parallel to the fibers in the case of matrix-dominated failure in compression. From these hypotheses, and taking into account that the composite lamina is isotropic in the 23 plane, Hashin [17] proposed a failure criteria which can be expressed as

$$\left[\left(\frac{Y_C}{2S_T}\right)^2 - 1\right]\frac{\sigma_2}{Y_C} + \left[\frac{\sigma_2}{2S_T}\right]^2 + \frac{\tau_{23}^2}{S_T^2} = 1 \qquad (1)$$

in the particular case of compression perpendicular to the fibers (σ_2) combined with shear stresses τ_{23} acting out of the lamina plane (Fig. 1). In this equation, Y_C and S_T stand for the lamina resistance to fracture subjected to transverse compression and out-of-plane shear, respectively. An analogous expression was derived for transverse compression and in-plane shear, but the experimental data for this loading condition did not always agree with the model predictions . In particular, Hashin's model did not capture the increase in shear strength in presence of moderate compressive stresses. This limitation was attributed to the fact that Hashin's model did not determine the actual orientation of the fracture plane but assumed a quadratic interaction between the stress invariants.

New models have been developed more recently to overcome these limitations. Among them, Puck [18,19] and LaRC03 criteria have been largely consistent with the experimental results available for failure under transverse compression and in-plane shear. Both criteria assume that failure is caused by the normal (σ_n) and tangential (τ_t) stresses acting on the failure plane, which forms an angle θ with the direction perpendicular to the compressive stresses, Fig. 1a. For the particular loading case considered in this paper, they are expressed as a function of the applied normal and shear stresses as

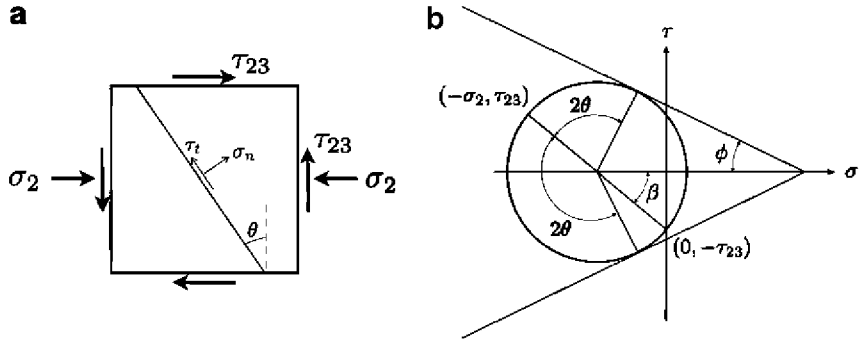

Fig. 1. (a) Stresses acting on the lamina and on the failure plane and (b) Mohr's circle for the stress state depicted in (a).

$$\sigma_n = \sigma_2 \frac{1 + \cos 2\theta}{2} + \tau_{23} \sin 2\theta \tag{2}$$

$$\tau_t = -\sigma_2 \frac{\sin 2\theta}{2} + \tau_{23} \cos 2\theta \tag{3}$$

$$|\tau_t| + \sigma_n \tan \phi = S_T \tag{4}$$

in which S_T, the fracture resistance of the fracture plane subjected to transverse shear, is assumed to be independent of the plane orientation θ, and ϕ stands for the friction angle which takes into account the influence of the normal stresses on the shear strength. The corresponding failure locus is determined by computing the actual orientation of the fracture plane for each combination of normal and tangential stresses on the lamina, which is given by the tangent point of the straight line which represents the Mohr–Coulomb criteria to Mohr's circle, as shown in Fig. 1b. Two fracture planes verify this condition, and their orientations with respect to the direction perpendicular to the compressive stress are given by

$$\theta = 45^\circ + \frac{\phi \pm \beta}{2} \tag{5}$$

in which $\beta = \arctan\{2\tau_{23}/\sigma_2\}$.

The practical application of these criteria is based on three material properties, namely Y_C, S_T and ϕ, but only Y_C can be easily measured in the laboratory. Nevertheless, if the Mohr–Coulomb model is accepted, the other two can also be obtained from the uniaxial transverse compression test as

$$\tan \phi = \frac{-1}{\tan 2\theta_c} \quad \text{and}$$

$$S_T = Y_c \cos \theta_c \left(\sin \theta_c + \frac{\cos \theta_c}{\tan 2\theta_c} \right) \tag{6}$$

in which θ_c is the orientation of the fracture plane under uniaxial compression. Experimental observations in many C/epoxy composites have shown that $\theta_c \approx 53 \pm 3^\circ$, and recent numerical simulations have demonstrated this angle is controlled by the matrix behavior in composites with good interfacial strength.

3. Virtual simulation strategy

The virtual simulations have to analyze the mechanical response of a composite lamina uniaxially reinforced with circular-section carbon fibers, which is subjected to normal compressive stresses in the transverse direction (either σ_2 or σ_3) and to shear stresses perpendicular to the fibers (τ_{23}), as shown in Fig. 2. Due to the symmetries of the material and of the loading conditions, the RVE selected was a square section of the lamina in the plane x_2x_3, perpendicular to the fibers, which contained a random dispersion of circular fibers (which covered 50% of the area) embedded in a matrix (Fig. 2). Previous analyses carried out under transverse compression have shown that RVEs with 30 fibers provide results very close to those obtained with 70 fibers, and accuracy improves if the overall behavior is obtained by averaging the stress–strain curves computed with various fiber distributions . Thus, RVEs containing random dispersions of thirty monosized fibers of radius $R = 5$ μm were generated in square RVEs of dimensions $L_0 \times L_0$ using the modified random sequential adsorption algorithm of Segurado and LLorca . It was assumed that the lamina's microstructure was given by an indefinite translation of the RVE along the x_2 and x_3 axes and, thus, the fiber positions within the RVE kept this periodicity condition. Fibers intersecting the RVE edges were

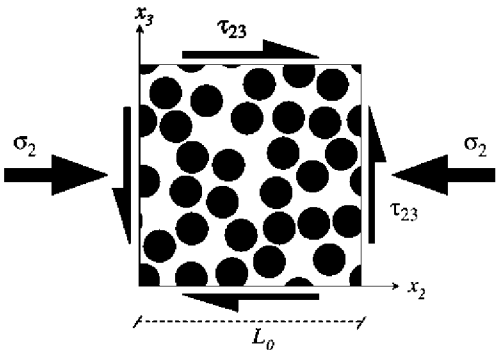

Fig. 2. Schematic of the representative volume element of the lamina microstructure subjected to combined transverse compression and out-of-plane shear.

split into an appropriate number of parts and copied to the opposite sides of the square RVE to create the periodic microstructure.

The mechanical behavior of the RVEs was studied using the finite element method. Matrix and fibers were automatically meshed using 6-node isoparametric modified triangles with integration at three Gauss points and hourglass control. In addition, 4-node isoparametric interface elements (COH2D4 in [25]) were inserted at the fiber/matrix interface in each fiber to include the effect of interface decohesion. The finite element discretization was fine enough throughout the RVE and included around 26,000 elements and 73,000 nodes to resolve the plastic shear bands in the matrix during deformation.

Periodic boundary conditions were applied to the edges of the RVE to ensure continuity between neighboring RVEs (which deform like jigsaw puzzles). The periodic boundary conditions can be expressed in terms of the displacement vectors $\vec{U}_2$ and $\vec{U}_3$ which relate the displacements between opposite edges according to

$$\vec{u}(0,x_3) - \vec{u}(L_0,x_3) = \vec{U}_2 \tag{7}$$

$$\vec{u}(x_2,0) - \vec{u}(x_2,L_0) = \vec{U}_3. \tag{8}$$

Combined uniaxial compression along the x_2 axis and shear deformation are imposed with $\vec{U}_2 = (-\delta_c, \delta_s)$ and $\vec{U}_3 = (u_2, u_3)$, where δ_c and δ_s stand for the imposed compressive and shear displacements, respectively. u_3 is computed from the condition that the average normal stresses perpendicular to the compression axis should be 0, and u_2 is determined from the condition of mechanical equilibrium. The compressive and shear strains are given by $\ln\{1 - \delta_c/L_0\}$ and $\arctan\{\delta_s/(L_0 - \delta_c)\}$, respectively, and the corresponding normal and shear stresses were computed from the resultant normal and tangential forces acting on the edges divided by the actual cross-section.

Simulations were carried out with Abaqus/Standard under plane strain conditions and within the framework of the finite deformations theory with the initial unstressed state as reference. For the loading conditions considered in this paper, the main stresses and strains in the fibers and in the matrix were in the 23 plane, while the stresses along the longitudinal 1 axis (due to Poisson effects) were, at least, one order of magnitude lower. Thus, although C fibers present very different properties in the longitudinal and transverse directions, they were modeled as linear, thermo-elastic and isotropic solids and their elastic constants perpendicular to the fiber axis were used in the simulations. They are given in Table 1.

Table 1
Elastic constants of the carbon fibers and of the epoxy matrix

E_f (GPa)	ν_f	E_m (GPa)	ν_m
20	0.25	4	0.35

The epoxy matrix was assumed to behave as an isotropic, elasto-plastic solid, and the elastic constants are also given in Table 1. Plastic deformation was governed by the Mohr–Coulumb criterion and the total matrix strain was given by the addition of the elastic and plastic strain components. The Mohr–Coulomb criterion assumes that yielding takes place when the shear stress acting on a specific plane, τ, reaches a critical value, which depends on the normal stress σ acting on that plane. This can be expressed as

$$\tau = c - \sigma \tan\phi \tag{9}$$

where c and ϕ stand, respectively, for the cohesion and the friction angle, two material parameters which control the plastic behavior of the material. Physically, the cohesion c represents the yield stress under pure shear while the friction angle takes into account the effect of the hydrostatic stresses. The Mohr–Coulomb model has often been used to describe plastic deformation of polymers because it accounts for the effect of hydrostatic pressure on the yield strength, and the development of plastic shear bands under compression .

According to the Mohr–Coulomb model, the matrix compressive strength, σ_{mc}, is given by

$$\sigma_{mc} = 2c\frac{\cos\phi}{1-\sin\phi} \tag{10}$$

and fracture under uniaxial compression takes place by the formation of a shear band which forms an angle $\theta_c = 45° + \phi/2$ with the plane perpendicular to the loading axis. Experimental results have shown that $\theta_c = 53 \pm 3°$ in epoxy-matrix composites , and thus $\phi = 15°$ is a sensible approximation. Assuming that the matrix compressive strength was 150 MPa , Eq. (10) leads to $c = 57.55$ MPa.

Finally, interface decohesion was included in the simulations through a cohesive crack model which dictates the fracture of the elements inserted at the fiber/matrix interface. The mechanical behavior of these elements was expressed in terms of a traction–separation law which relates the displacement jump across the interface with the traction vector acting upon it . The interface elements initially provide a linear, stiff response which ensures the displacement continuity at the interface. An elastic stiffness of 10^8 GPa/m was selected for the interface, which was large enough to ensure the displacement continuity at the interface and to avoid any modification of the stress fields around the fibers in the absence of damage . The onset of damage is dictated by a maximum stress criterion expressed mathematically as

$$max\left\{\frac{\langle t_n\rangle}{N}, \frac{t_s}{S}\right\} = 1 \tag{11}$$

in which $\langle\rangle$ stand for the Macaulay brackets, which return the argument if positive and zero otherwise, to impede the development of damage when the interface is under compression, and N and S are the normal and tangential

interfacial strengths which for simplicity were assumed to be equal ($N = S$).

Once the damage begins, the stress transferred through the crack is reduced depending on the interface damage parameter d, which evolves from 0 (in the absence of damage) to 1 (no stresses transmitted across the interface) following a linear traction–separation law. In addition, the energy necessary to completely break the interface is always equal to Γ, the interface fracture energy, regardless of the loading path. It has been shown previously that the compressive strength of fiber-reinforced composites is very sensitive to the interface strength but not to the interface toughness . Thus, results for two different materials are presented below, the first with a strong interface ($N = S = c$) and the second with a weak one ($N = S = 0.25c$). In both cases, the interface fracture energy was 100 J/m^2 , a reasonable magnitude for C/epoxy interfaces according to available experimental data. More details about the numerical implementation of the Mohr–Columb and cohesive crack models can be found in a previous investigation .

4. Results

4.1. Composite with a strong interface

Different fiber realizations were generated using the strategy described above, leading to a homogeneous, random and isotropic distributions of fibers in the RVE, which were statistically equivalent although the precise location of the fibers was different in each one. The stress–strain curves under uniaxial compression and pure shear are plotted in Fig. 3 for the composite material with a strong interface ($N = S = c$). The calculations were stopped (or finished due to numerical instabilities) after the maximum load was attained. The results for six different realizations of the fibers within the RVE presented in this figure show very little scatter up to the maximum load (Table 2), indicating that the size of the RVE was large enough to compute the lamina strength. The samples loaded in uniaxial compression attained the maximum load at compressive strains in the range −2% to −3%. The contour plot of the plastic strains in the matrix (Fig. 4) showed that failure took place by the propagation of a shear band in the matrix. The shear band cannot propagate though the fibers, leading to slight variations in the orientation, which are controlled by the details of the fiber arrangement. The average orientation of the fracture plane, θ_c, was 48.9° ± 1.9°, slightly lower than 52.5°, the theoretical value predicted by Eq. (5) for a Mohr–Coulomb material with $\phi = 15°$. Previous analyses have shown that failure in transverse compression took place in the absence of interface decohesion by the nucleation and propagation of a network of plastic shear bands in the matrix oriented at $\theta \approx \pm 52.5°$. Interface cracks promoted the localization of damage in one single shear band, whose precise orientation depended on the details of the fiber spatial distribution, and that did not always grow along the theoretical angle. It should be noted that the predictions of these numerical simulations for transverse compression presented in [16] were in excellent agreement with the experimental observations in [26,29] in terms of the compressive strength, the ductility and the dominant failure mechanism.

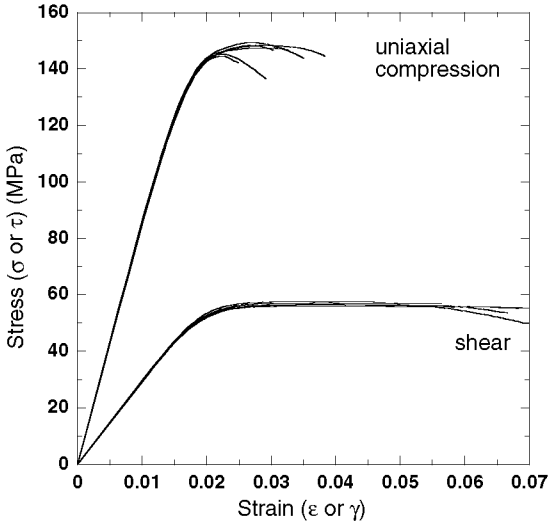

Fig. 3. Stress–strain curves under uniaxial compression and out-of-plane shear for the composite lamina with a strong fiber/matrix interface. The absolute values of the stress and strain are used to plot the curves in compression.

The stress–strain curve in shear presented a wide plateau and the maximum was attained for shear strains in the range 2–4%, although the differences in the maximum shear strength were negligible (Table 2). The analysis of the contour plot of the accumulated plastic strain in the matrix showed that failure also took place by the propagation of a dominant plastic shear band in the matrix in which most of the plastic strain was localized after the peak stress (Fig. 5). The average orientation of the fracture plane, θ_s, was 8.4° ± 2.3°, slightly higher than $\phi/2$ (= 7.5°), the theoretical value predicted for a Mohr–Coulomb material deformed in pure shear. Once again, these minor discrepancies can be attributed to the influence of interface decohesion which promotes the localization of fracture in one dominant shear band.

The simulations to study the behavior under combined compression and shear were carried out with a fixed ratio

Table 2
Stresses at failure under different loading conditions for the composite with a strong interface

Loading mode	Uniaxial compression	Shear	$\delta_c/\delta_s = -1/8$
σ_2 (MPa)	−147.2 ± 1.9	–	−28.2 ± 2.5
τ_{23} (MPa)	–	56.7 ± 0.6	58.4 ± 0.8

The results in the table are the average and standard deviation over six different realizations.

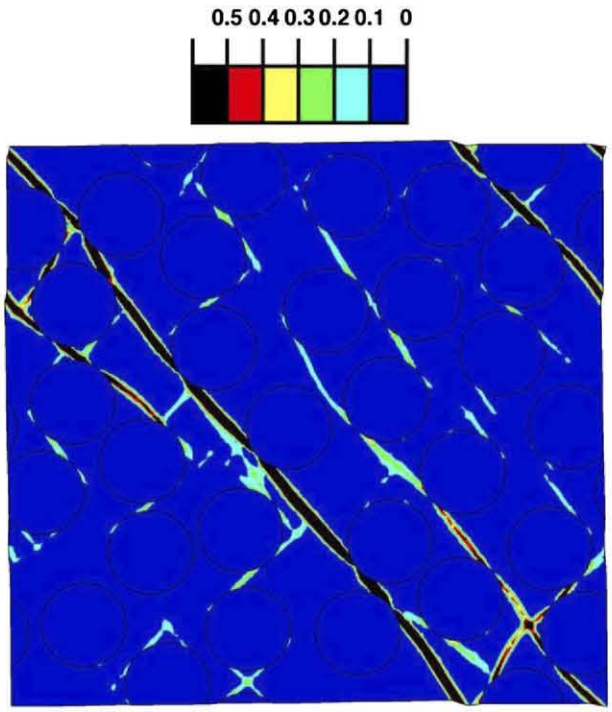

Fig. 4. Contour plot of the accumulated plastic strain in the composite with a strong interface subjected to uniaxial compression in the vertical direction. The plastic strain corresponding to each color is shown in the legend. The applied strain was −3.2%.

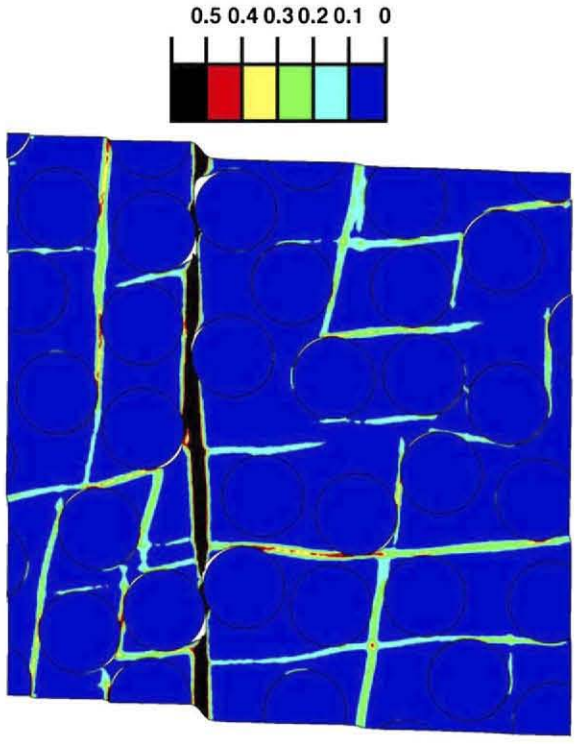

Fig. 5. Contour plot of the accumulated plastic strain in the composite with a strong interface subjected to pure shear. The applied strain was 7.1%.

of the normal displacement to the shear displacement. The $\sigma - \epsilon$ and $\tau - \gamma$ curves corresponding to six different fiber realizations are plotted in Fig. 6a in the case $\delta_c/\delta_s = -1/8$. The scatter in the results obtained with different RVEs was limited (Table 2), as in the cases of uniaxial compression and shear. For this particular δ_c/δ_s ratio, the $\sigma - \epsilon$ curve was fairly linear while the $\tau - \gamma$ response was non-linear and presented a maximum. The evolution of the shear stress with the compressive stress for different δ_c/δ_s ratios (from −1/50 to −2) is plotted in Fig. 6b for one RVE. A maximum in the shear stress was found in all cases, and this maximum was sharper and followed by a larger drop as the amount of shear deformation increased over the compressive strain. A maximum in the compressive stress was only found when $\delta_c/\delta_s = -2$ and it was followed by a marked reduction in the compressive stress indicating that failure by compression (instead of shear) was dominant in this case.

From the physical viewpoint, the composite's deformation under combined shear and compression was initially controlled by the formation of two sets of bands of intense plastic deformation in the matrix (Fig. 7). The orientation of these bands was measured in two different RVEs which were subjected to different ratios of compressive and shear deformation. The average values (and the standard deviations) are plotted in Fig. 6c as a function of the ratio between shear and compressive stresses τ_{23}/σ_2 at failure (which was dictated by the maximum in shear). They are consistent with the predictions of the Puck and LaRC models, Eq. (5), and demonstrate that these simple physically-based models capture composite behavior very well when it is dominated by the matrix. Final fracture occurred by the localization of plastic deformation in the matrix along one dominant shear band (Fig. 7). The precise orientation of the fracture plane was dictated by the details of the fiber arrangement in the RVE and the combination of normal and shear stresses applied, and was not always consistent with the predictions of Mohr–Coulomb theory.

Assuming that failure occurs when a maximum in the compressive or shear stress is attained, the corresponding failure envelope can be built from the simulations of the RVEs subjected to uniaxial compression, shear and combined shear and compression. They were obtained for different δ_c/δ_s ratios on two RVEs and the average value is plotted in Fig. 8, together with the predictions of failure criteria developed by Hashin , Puck and Schürmann and Dávila . The curves corresponding to these criteria were obtained by introducing the numerical value of the strength in uniaxial compression (see Table 2) and $\theta_c = 53°$ in Eqs. (1) and (4). They were in fairly good agreement with the numerical results. In particular, Hashin's model was practically superposed to the numerical data, and this behavior was unexpected because this model did not predict the increase in shear strength under moderate compressive stresses found under combined compression and in-plane shear (σ_2 and τ_{12}) . Hashin's model assumes that failure is controlled by a quadratic interaction

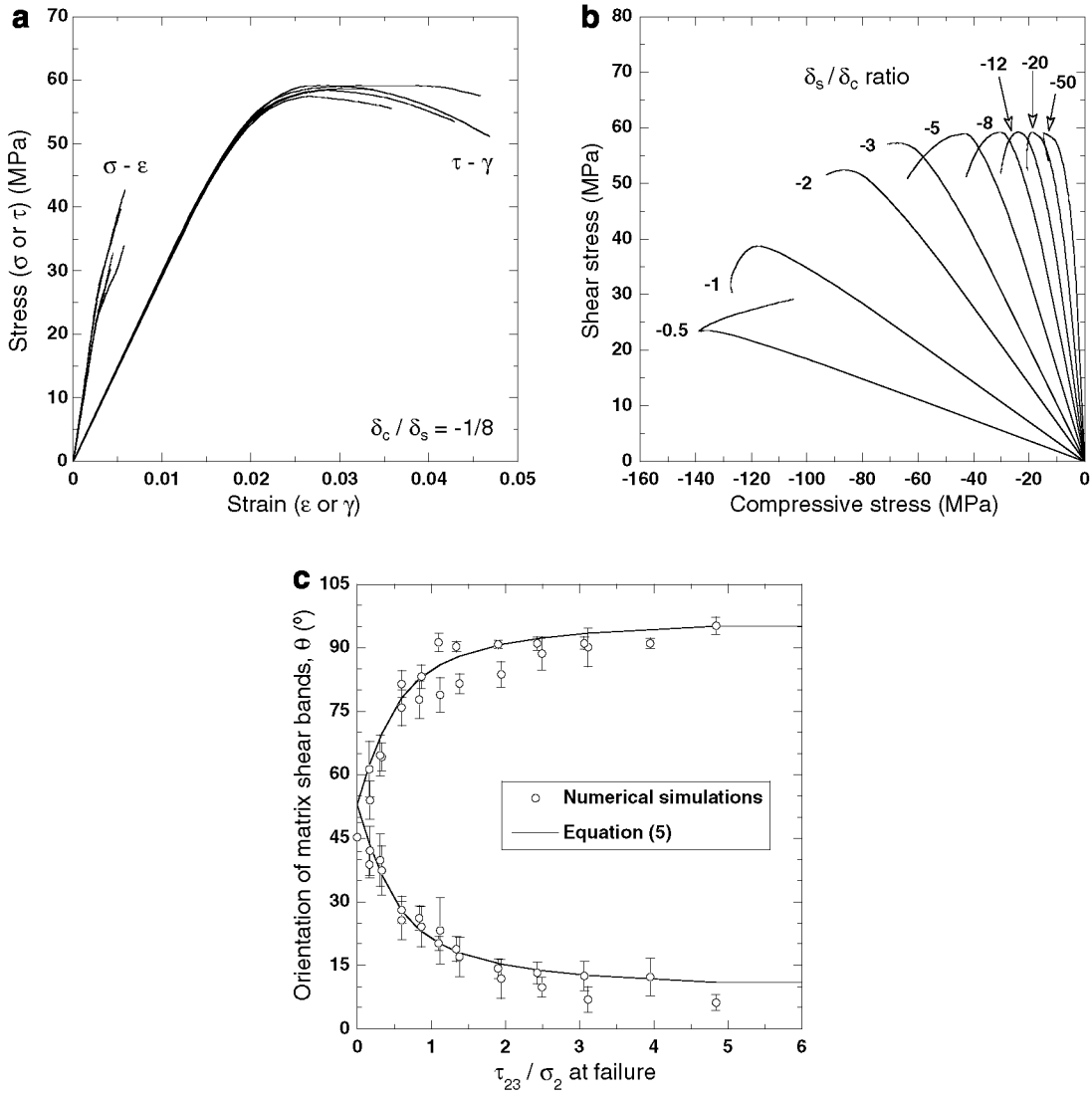

Fig. 6. Mechanical response of the composite with a strong interface under combined transverse compression and shear: (a) $\sigma - \epsilon$ and $\tau - \gamma$ curves corresponding to five different fiber realizations in the case $\delta_c/\delta_s = -1/8$, (b) evolution of the shear stress τ with the compressive stress σ for different δ_c/δ_s ratios and (c) orientation of the plastic shear bands in the matrix with respect to the direction perpendicular to the compression axis as a function of the ratio between shear and compressive stresses at failure. The orientation of the shear bands under pure shear (not included in the plot) was $7.8 \pm 4.2°$ and $95.1 \pm 2.0°$. The theoretical predictions from Puck and LaRC models (Eq. (5)) are plotted together with the results of the numerical simulations.

between the normal and shear stresses but this hypothesis is not appropriate to reproducing the behavior under transverse compression and in-plane shear when the latter is dominant. Failure occurs along the plane of maximum shear stress ($\theta = 0°$) under these conditions and the strength increases linearly with transverse compression, as predicted by the Mohr–Coulomb model. For the loading mode considered here, transverse compression and out-of-plane shear, the orientation of the failure plane depends on the magnitude of the normal and shear stresses, and the quadratic interaction approximation proposed by Hashin is very accurate.

Puck and LaRC models also adequately reproduce the shape of the failure surface and predict a maximum in the shear strength for small amounts of transverse compression, consistent with the numerical simulations. In addition, the orientation of the shear bands in the matrix according to the Mohr–Coulomb's model coincide with the numerical predictions, and this demonstrates that they capture the actual fracture mechanisms in the composite well. Discrepancies in the magnitude of the strength in the shear-dominated region of the failure diagram can be attributed to the presence of interface decohesion in the numerical simulations, which is not accounted for in the failure criteria. Nevertheless, this discrepancy is small in the case of composites with good interfacial strength. It should be noticed that both Puck and LaRC models have been in reasonable good agreement with the experimental results of the World Wide Failure Exercise for unidirectional lamina subjected to transverse compression and in-plane shear. Their predictions are validated here against our virtual tests for another multiaxial stress state given

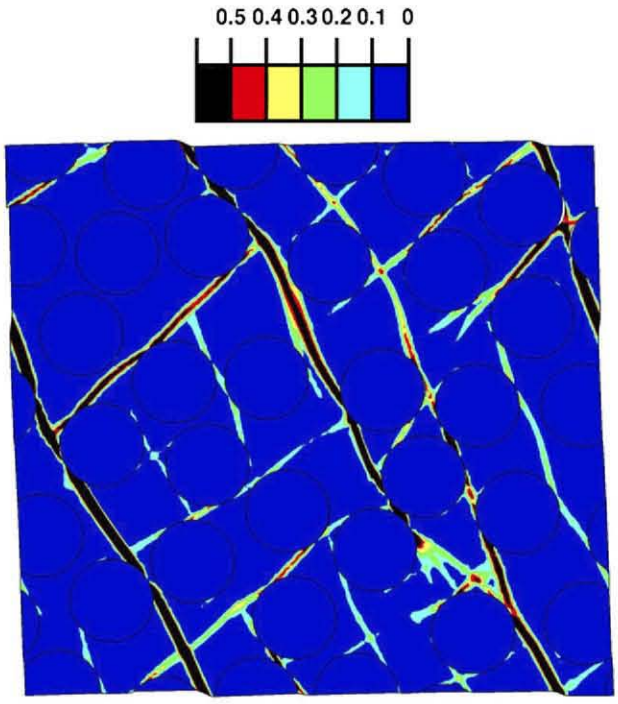

Fig. 7. Contour plot of the accumulated plastic strain in the composite with a strong interface subjected to combined vertical compression and shear in the case $\delta_c/\delta_s = -1$. The applied shear and compressive strains were 3.66% and −3.60%, respectively.

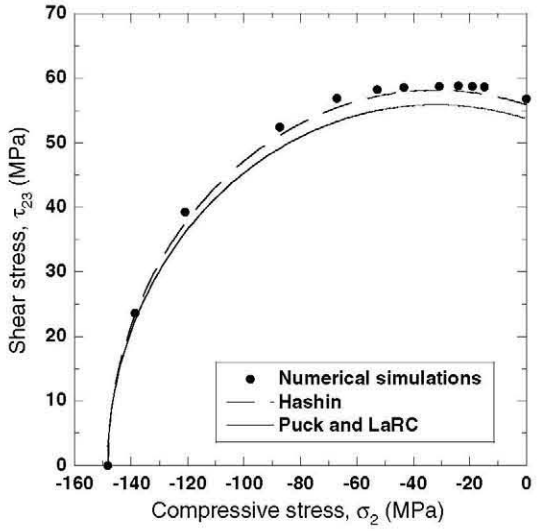

Fig. 8. Failure surface of the composite with a strong interface subjected to transverse compression and out-of-plane shear. The results of the numerical simulations are plotted together with those obtained from Hashin – Eq. (1) – and Puck and LaRC criteria – Eq. (4).

by transverse compression and out-of-plane shear, which is difficult to reproduce experimentally.

4.2. Composite with a weak interface

As indicated in the introduction, failure criteria for composites distinguish between matrix- and fiber-dominated fracture modes but they do not take into account the interface properties. This may be partially due to the limited amount of reliable experimental data on the interface properties , but it is well established that sizing treatments on the fiber surface or environmental conditions, for instance, can dramatically modify the interface strength. The influence of interface decohesion in the fracture process was addressed by repeating the numerical simulations presented above in composites with a weak interface, whose strength was given by $N = S = 0.25c$. They were aimed at elucidating the influence of this factor on the accuracy of the current failure criteria for composites.

The stress–strain curves of six different fiber realizations under uniaxial compression and pure shear are plotted in Fig. 9. The simulations presented very little scatter up to the maximum load in both cases, indicating that the size of the RVE is large enough to compute the failure strength in compression and shear (Table 3). The comparison between Figs. 3 and 9 and Tables 2 and 3 shows that the presence of a weak interface leads to a marked non-linearity in the stress–strain curves in compression and shear, and significantly reduces the strength, particularly in shear. The origin of these differences can be understood from the contour plots of accumulated plastic strain in the matrix shown in Figs. 10 and 11 for uniaxial compression and shear, respectively. Failure is initiated by the nucleation of interface cracks, which give rise to the non-linear behavior at small strains, and damage progresses by the formation of bands of intense plastic deformation in the matrix which link up the interface cracks. This is particularly clear in Fig. 11, in which most of the applied shear strain has been concentrated in a band formed by successive interface cracks which provided a weak path for the localization of damage. This marked localization was very sensitive to

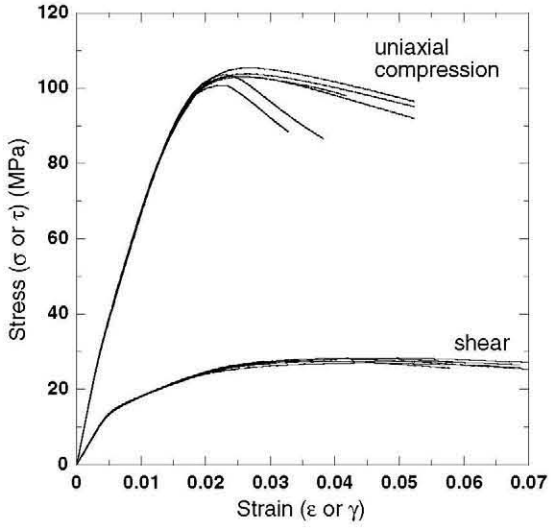

Fig. 9. Stress–strain curves under uniaxial compression and out-of-plane shear for the composite lamina with a weak fiber/matrix interface. The absolute values of the stress and strain are used to plot the curves in compression.

Table 3
Stresses at failure under different loading conditions for the composite with a weak interface

Loading mode	Uniaxial compression	Shear	$\delta_c/\delta_s = -1/8$
σ_2 (MPa)	-103.2 ± 1.5	–	-35.9 ± 2.1
τ_{23} (MPa)	–	27.7 ± 0.5	32.6 ± 0.4

The results in the table are the average and standard deviation over six different realizations.

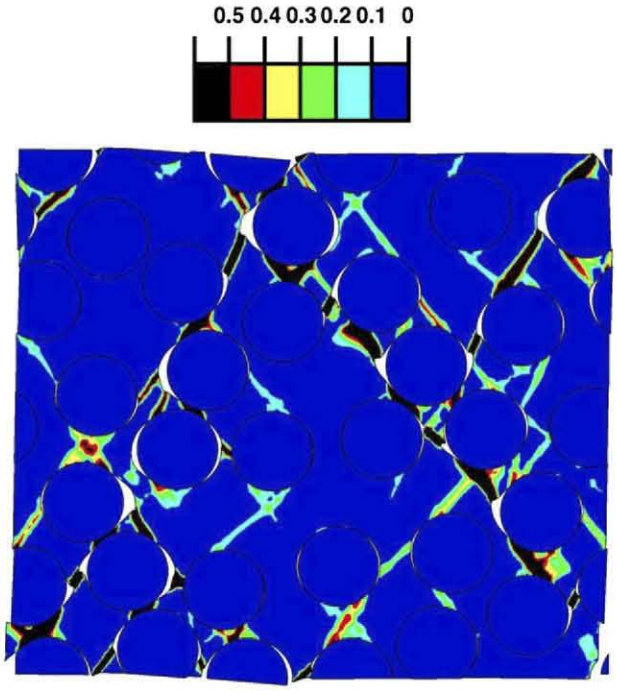

Fig. 10. Contour plot of the accumulated plastic strain in the composite with a weak interface subjected to uniaxial compression in the vertical direction. The applied strain was −5.7%.

the actual distribution of the fibers in the RVE, and it was responsible for the significant differences in the stress–strain curve after the peak stress sometimes observed among various fiber realizations (Fig. 9). It is obvious from the results in Figs. 10 and 11 that the orientation of the fracture planes has nothing to do with the predictions of the Mohr–Coulomb model. Although the matrix follows this criterion, the composite does not because the weak interface controls the fracture process.

Behavior under combined compression and shear is summarized in Fig. 12. The $\sigma - \epsilon$ and $\tau - \gamma$ curves corresponding to six different fiber realizations in the case $\delta_c/\delta_s = -1/8$ are plotted in Fig. 12a. A maximum in the shear and compressive stress was found for this combination of normal and shear deformation, while only a maximum in shear was obtained in the composites with a strong interface. This behavior was general for all combinations of compressive and shear stresses, as shown in Fig. 12b, in which the evolution of the shear stress with the compressive stress for different δ_c/δ_s ratios (from $-1/50$ to -2) is plotted for one RVE. The first maximum was attained for the shear

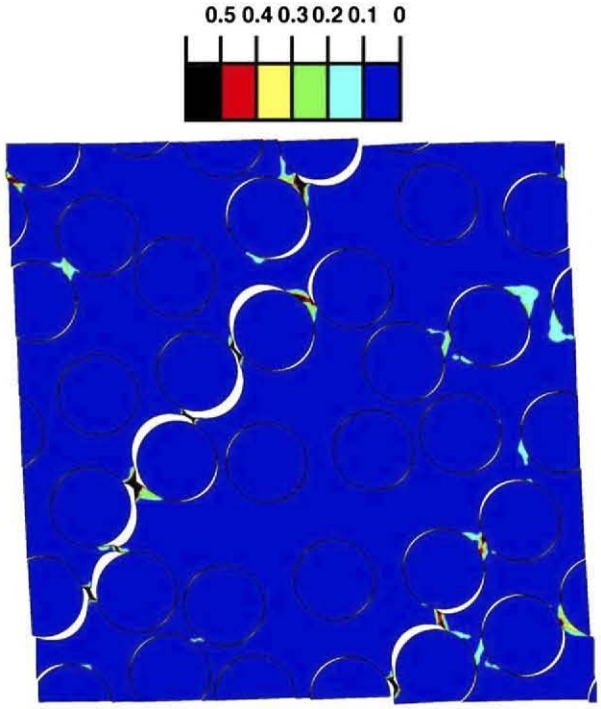

Fig. 11. Contour plot of the accumulated plastic strain in the composite with a weak interface subjected to pure shear. The applied strain was 5.2%.

stress, and it was followed by a maximum in the compressive stress. The contour plots of the accumulated plastic strain the matrix under combined compression and shear (not plotted for sake of brevity) showed similar features to those shown in Figs. 10 and 11: failure was dominated by the formation of bands of intense plastic deformation in the matrix which linked up interface cracks.

Assuming that failure occurs when a maximum in the shear stress is attained, the corresponding failure envelope can be built from the simulations of the RVEs subjected to uniaxial compression, shear and combined shear and compression. They were computed for different δ_c/δ_s ratios on two RVEs and the average value is plotted in Fig. 13, together with the predictions of failure criteria developed by Hashin , Puck and Schürmann and Dávila . As in the case of the composites with strong interfaces, the curves corresponding to these criteria were obtained by introducing the numerical value of the strength in uniaxial compression (see Table 3) and $\theta_c = 53°$ in Eqs. (1) and (4). Neither criterion adequately predicts the failure strength of the composite, and all of them overestimate strength in the region dominated by shear stresses. This result is not surprising because the effect of a weak interface on the strength is more severe in shear than in compression, and this anisotropy cannot be captured by a criterion based on a quadratic interaction between normal and shear stresses, like the one proposed by Hashin. In addition, composite fracture is not controlled by the Mohr–Coulomb theory and the models based on this assumption are no longer capable of predicting the failure stress accurately.

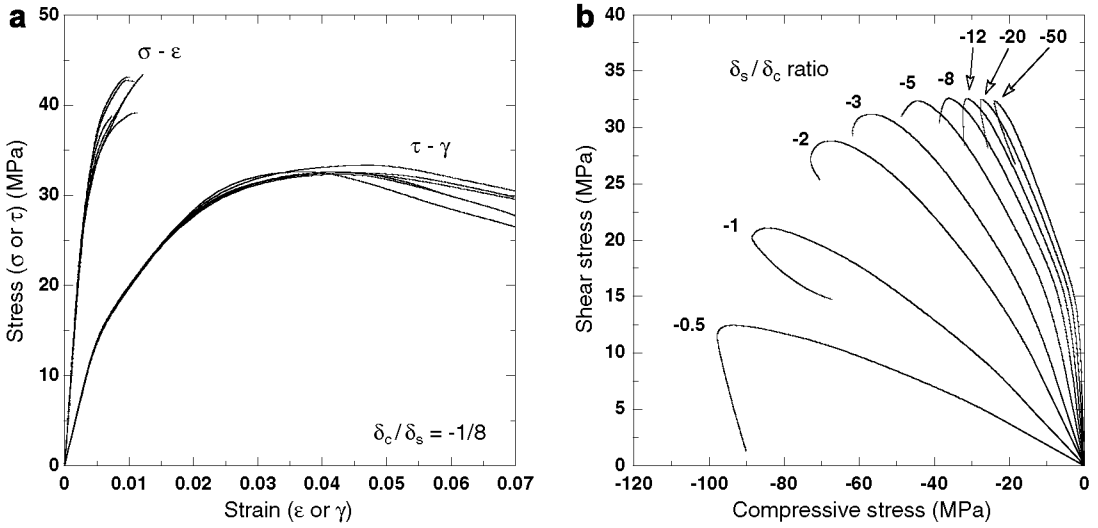

Fig. 12. Mechanical response of the composite with a weak interface under combined transverse compression and shear: (a) $\sigma - \epsilon$ and $\tau - \gamma$ curves corresponding to six different fiber realizations in the case $\delta_c/\delta_s = -1/8$ and (b) evolution of the shear stress τ with the compressive stress σ for different δ_c/δ_s ratios.

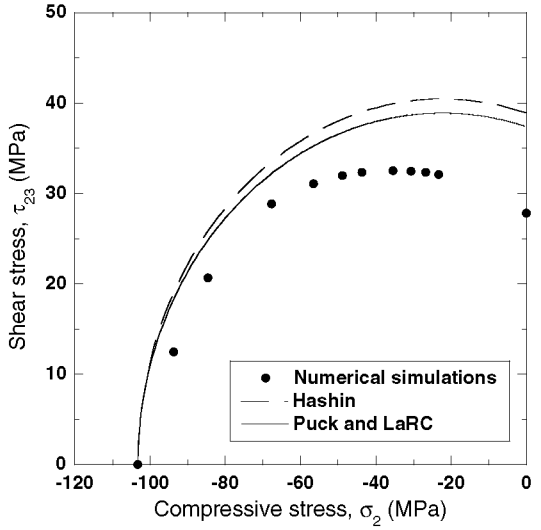

Fig. 13. Failure surface of the composite with a weak interface subjected to transverse compression and out-of-plane shear. The results of the numerical simulations are plotted together with those obtained from Hashin – Eq. (1) – and Puck and LaRC criteria – Eq. (4).

5. Concluding remarks

The mechanical behavior of a fiber-reinforced composite lamina under transverse compression and out-of-plane shear has been simulated using computational micromechanics. This strategy explicitly takes into account fiber and matrix spatial distribution within the lamina as well as matrix, fiber and interface properties which are included in the simulations through the corresponding constitutive models. The results presented in this paper show that this strategy is able to accurately reproduce the physical fracture mechanisms experimentally observed, and opens the possibility of replacing (at least partially) costly and time-consuming mechanical tests by virtual tests. These virtual tests present several advantages over the standard experimental approach, which include full control of the composite microstructure and of the constituent properties (eliminating major sources of uncertainty and scatter), the potential to reproduce very complex stress states with well-defined boundary conditions, and the ability to carry out systematic parametrical studies to optimize composite properties. Of course, further validation of this technique is necessary to gain in confidence and to assess its limitations. One step in this direction is developed in this paper: the validation of the failure criteria for composite lamina under a multiaxial stress state (transverse compression and out-of-plane shear), whose experimental reproduction is highly complex.

In the case of composites with good fiber/matrix interfacial strength, the failure locus computed from the numerical simulations was consistent with the Hashin , Puck and LaRC failure criteria, in which the only experimental parameter was the strength of the composite lamina under transverse compression, Y_C. The numerical simulations showed that failure took place by the localization of the plastic strain in the matrix in a shear band, whose orientation for each combination of normal and shear stresses was close to the one predicted by Puck and LaRC models. The ability of these models, based on the stress state in the lamina and the Mohr–Coulomb criterion for matrix failure, to reproduce physical fracture mechanisms supports the reliability of their predictions to assess the failure of composite lamina.

In the case of composites with a weak fiber/matrix interface, the simulations showed that the dominant failure mechanism was interface decohesion rather than matrix plastic deformation. Final fracture occurred by the link up of interface cracks nucleated at the early stages of

deformation through the matrix, and the influence of the weak interfaces on strength was much more severe in shear than in compression. The predictions of the three failure criteria (which were based as before on the strength of the composite lamina under transverse compression) overestimated the composite strength in shear and they cannot be used to predict the mechanical behavior of composites with a weak interface. The numerical simulations point out that a new failure mode, namely interface decohesion, has to be taken into account to develop failure criteria for composites in "matrix"-dominated failure modes and, perhaps, if the dominant fracture mode is fiber fracture in compression. Of course, this contribution is small when the interface strength is higher than the matrix but it may become dominant otherwise.

Acknowledgements

This investigation was supported by the Ministerio de Eduación y Ciencia de España through the grant MAT 2006-2602 and by the Comunidad de Madrid through the program ESTRUMAT-CM (reference MAT/0077).

References

Thomason PF. Ductile fracture of metals. Pergamon Press; 1990.
Flores KM. Structural changes and stress state effects during inhomogeneous flow of metallic glasses. Scripta Mater 2006;54:327–32.
Lund AC, Schuh CA. Yield surface of a simulated metallic glass. Acta Mater 2003;51:5399–411.
Sternstein SS. Yielding in glassy polymers. In: Polymeric materials. American Society for Metals; 1975. p. 369–89.
Argon AS. A theory for the low-temperature plastic deformation of glassy polymers. Philos Mag 1973;28:839–65.
Hinton MJ, Soden PD, Kaddour AS. Failure criteria in fiberreinforced polymer composites: the world wide failure exercise. Elsevier; 2004.
Vogler TJ, Hsu S-Y, Kyriakides S. Composite failure under combined compression and shear. Int J Solids Struct 2000;37:1765–91.
Soden PD, Hinton MJ, Kaddour AS. A comparison of the predictive capabilities of current failure theories for composite laminates. Compos Sci Technol 1998;58:1225–54.
Kaddour AS, Hinton MJ, Soden PD. A comparison of the predictive capabilities of current failure theories for composite laminates: additional contributions. Compos Sci Technol 1998;58:1225–54.
Cox B, Yang Q. In quest of virtual tests for structural composites. Science 2006;314:1102–7.
Segurado J, LLorca J. A computational micromechanics study of the effect of interface decohesion on the mechanical behavior of composites. Acta Mater 2005;53:4931–42.
Segurado J, LLorca J. Computational micromechanics of composites: the effect of particle spatial distribution. Mech Mater 2006;38:873–83.
LLorca J, Segurado J. Three-dimensional multiparticle cell simulations of deformation and damage in sphere-reinforced composites. Mater Sci Eng 2004;A365:267–74.
González C, LLorca J. Multiscale modeling of fracture in fiber-reinforced composites. Acta Mater 2006;54:4171–81.
González C, LLorca J. Virtual fracture testing of fiber-reinforced composites: a computational micromechanics approach. Eng Fract Mech 2007;74:1126–38.
González C, LLorca J. Mechanical behavior of unidirectional fiberreinforced polymers under transverse compression: microscopic mechanisms and modeling. Compos Sci Technol 2007;67:2795–806.
Hashin Z. Failure criteria for unidirectional fiber composites. J Appl Mech 1980;47:329–34.
Puck A, Schürmann H. Failure analysis of FRP laminates by means of physically based phenomenological models. Compos Sci Technol 1998;58:1045–67.
Puck A, Schürmann H. Failure analysis of FRP laminates by means of physically based phenomenological models. Composites Sci Technol 2002;62:1633–62.
Dávila C, Camanho PP, Rose CA. Failure criteria for FRP laminates. J Compos Mater 2005;39:323–45.
Pinho ST, Iannucci L, Robinson P. Physically-based failure models and criteria for laminated fibre-reinforced composites with emphasis on fibre-kinking. Part I: devlopment. Compos: Part A 2006;37:63–73.
Hine PJ, Lusti HR, Gusev AA. Numerical simulation of the effects of volume fraction, aspect ratio and fibre length distribution on the elastic and thermoelastic properties of short fibre composites. Compos Sci Technol 2002;62:1445–53.
Segurado J, González C, LLorca J. A numerical investigation of the effect of particle clustering on the mechanical properties of composites. Acta Mater 2003;51:2355–69.
Segurado J, LLorca J. A numerical approximation to the elastic properties of sphere-reinforced composites. J Mech Phys Solids 2002;50:2107–21.
Abaqus, Users' Manual, ABAQUS, Inc.; 2006.
Soden PD, Hinton MJ, Kaddour AS. Lamina properties, lay-up configurations and loading conditions for a range of fibre-reinforced composite laminates. Compos Sci Technol 1998;58:1011–22.
Kinloch AJ, Young RJ. Fracture behavior of polymers. Elsevier Applied Science; 1983.
Rabinowitz S, Ward IM, Perry JSC. The effect of hydrostatic pressure on the shear yield behavior of polymers. J Mater Sci 1970;5:29–39.
Aragonés D. Fracture micromechanisms in C/epoxy composites under transverse compression. Master thesis, Universidad Politécnica de Madrid; 2007.
Zhou X-F, Wagner HD, Nutt SR. Interfacial properties of polymer composites measured by push-out and fragmentation tests. Compos: Part A 2001;32:1543–51.
Kim J-K, Mai YW. Engineered interfaces in fiber reinforced composites. Elsevier; 1998.
González C, LLorca J. Numerical simulation of the fracture behavior of Ti/SiC composites between 20 °C and 400 °C. Metall Mater Trans A 2007;38:169–79.